Post-Print

This is the accepted version of:

The final publication is available at https://doi.org/10.1016/j.asr.2019.03.001

Access to the published version may require subscription.

When citing this work, cite the original published paper.

Permanent link to this version
http://hdl.handle.net/11311/1139190

A Numerical Approach to the Problem of Angles-Only Initial Relative Orbit Determination in Low Earth Orbit

Jean-Sébastien Ardaens[1], Gabriella Gaias

DLR, German Aerospace Center, 82234 Wessling, Germany

Abstract

A practical and effective numerical method is presented, aiming at solving the problem of initial relative orbit determination using solely line-of-sight measurements. The proposed approach exploits the small discrepancies which can be observed between a linear and a more advanced relative motion model. The method consists in systematically performing a series of least-squares adjustments at varying intersatellite distances in the vicinity of a family of collinear solutions coming from the linear theory. The solution presenting the smallest fitting residuals is then selected. The investigations specifically focus on the rendezvous in low Earth near-circular orbit with a noncooperative target. The objective is to determine the relative state of the formation using only bearing observations when the spacecraft are separated by a few dozen kilometers without any a-priori additional information. The method is validated with flight data coming from the ARGON (2012) and AVANTI (2016) experiments. Both cases demonstrate that an observation time span of a few maneuver-free orbits is enough to compute a solution which can compete with Two-Line Elements in terms of accuracy.

Keywords: angles-only navigation; noncooperative rendezvous; formation-flying; flight demonstration; initial orbit determination

1. Introduction

The determination of the trajectories of celestial objects based on line-of-sight measurements is an ancient and well-established technique. Gauss

---

Email address: `jean-sebastien.ardaens@dlr.de` (Jean-Sébastien Ardaens)
[1]Corresponding author.

and Laplace already addressed this problem more than 200 years ago when observing asteroids (Gauss, 1809). More recently, it has been recognized that angles-only navigation could also be a powerful method to track noncooperative objects in space from a satellite (Chari, 2001; Woffinden, 2008). In this case, the observer is no longer located on Earth but is also orbiting, creating a new difficulty: the relative navigation problem becomes weakly observable if both observer and tracked object are flying on similar orbits.

A particular use case of angles-only relative navigation consists in employing a single monocular camera to rendezvous in space with a noncooperative object. Over the last few years, the German Space Operations Center (DLR/GSOC) has dedicated considerable efforts in this research field. Two in-orbit demonstrations with increasing complexity have been conducted to collect relevant flight experience. The first experiment, called ARGON (Advanced Rendezvous demonstration using GPS and Optical Navigation), took advantage of the PRISMA formation-flying testbed (Persson et al., 2005) to demonstrate in 2012 the ability to perform a far- to mid-range ground-in-the-loop rendezvous with a noncooperative target, reducing the intersatellite separation from 30 km to 3 km (D'Amico et al., 2013). Based on this experience, a second more challenging endeavor was conducted in 2016: the AVANTI (Autonomous Vision Approach Navigation and Target Identification) experiment, which successfully demonstrated the ability to autonomously rendezvous with a fully noncooperative spacecraft (Gaias and Ardaens, 2018). AVANTI has been implemented on the BIROS satellite (Halle et al., 2014), which was chasing a picosatellite named BEESAT-4 (Baumann et al., 2012) from 50 km to only 50 m separation.

Both experiments solely relied on images taken by a monocular camera to estimate the relative motion. However, due to the weak observability of the problem, the provision of an *a priori* coarse solution was required to ensure the convergence of the estimation techniques. This Initial Relative Orbit Determination (IROD) has been done using Two-Line Elements (TLE) and was employed to initialize the on-ground precise angles-only relative orbit determination (supporting the ARGON (Gaias et al., 2014) and AVANTI (Ardaens and Gaias, 2018a) experiments) and the on-board autonomous real-time relative navigation filter (used only for AVANTI, see Ardaens and Gaias (2018b)). This was justified by the fact that a rendezvous in space is always done with a target object which is not unknown, so that coarse orbit information is always available. Still, it remains an interesting research question to investigate if the use of TLEs could have been entirely avoided. This

would have simplified the interfaces, making the relative navigation task independent from external additional information. Moreover, this would have contributed to increase the autonomy level of the spaceborne rendezvous system employed during the AVANTI experiment.

The problem of IROD has recently attracted considerable attention. Section 2.2 provides an overview of the current research directions in this domain. All these activities are of great relevance, since they provide the theoretical justification of possible approaches to improve the observability property of the relative orbit determination problem. This work intends to complement this fundamental research by providing a quantitative analysis based on flight data and experience collected during the ARGON and AVANTI experiments, which were both conducted in low Earth orbits (LEO). The objective consists in determining the relative trajectory of objects flying on near-circular orbits, with applicability to in-space debris monitoring, active debris removal or on-orbit servicing activities. Note that these topics are currently of primary interest, given the density and natural evolution of the population of objects flying in the LEO belt (Liou and Johnson, 2008; Liou, 2011). A second contribution of this study regards the domain of applicability of the proposed solution in terms of relative range. From an operational point of view, in fact, IROD has to be performed when the spacecraft are separated by a few dozen of kilometers, as it would be too dangerous to start estimating the relative state only at few hundred meters of distance. On the other hand, working with too large separations (a few hundred kilometers) poses the problem of detectability of the target, a technological constraint driven by the sensor capabilities. As explained more in details in the next section, these practical considerations limit the domain of applicability of some of the theoretical methods designed to perform at close or very large distances. The experience gained with AVANTI indicates that a small picosatellite would not have been visible at such distances (in fact, it was barely visible at 50 km separation, *cf.* Ardaens and Gaias (2018a)).

After a brief description of the observability problem, the different approaches proposed in the literature for IROD are reviewed in Section 2. A new method is then introduced to numerically solve this problem. Section 3 provides an analysis of the factors influencing the solution in terms of accuracy. These investigations are conducted by the means of simulations, which allow for individual and systematical activation of key parameters and perturbations. Finally, Section 4 shows how this numerical method performs on two different cases taken from the AVANTI and ARGON experiments.

3

2. Initial Relative Orbit Determination

2.1. Woffinden's Dilemma

The problem of angles-only relative navigation consists in finding the relative state (*i.e.*, position and velocity) between a target and a chaser spacecraft corresponding to a given set of n line-of-sight measurements $\{\boldsymbol{u}_i\}$ taken at times t_i. These observations are unit vectors directed to the target object, and can equivalently be parameterized by a set of two angles (for example right-ascension and declination, or azimuth and elevation). It is well-known that this problem is weakly observable. Woffinden and Geller (2009a) elegantly demonstrated that, under the assumption of an homogeneous linear relative motion with a linear measurement model, the relative motion is even not observable. The demonstration is quickly recalled here for completeness. Let $\boldsymbol{x}(t)$ denote the relative state at time t (either in a Cartesian frame or parameterized with relative orbital elements). A linear relative motion model implies that

$$\boldsymbol{x}(t) = \boldsymbol{\Phi}(t, t_0) \cdot \boldsymbol{x}(t_0), \tag{1}$$

where $\boldsymbol{\Phi}(t, t_0)$ is the state transition matrix between an initial epoch t_0 and t. Let assume that the relative position $\boldsymbol{r}(t)$ has a linear dependency to the state vector $\boldsymbol{x}(t)$ (which is trivial if $\boldsymbol{x}$ is formulated in the Cartesian frame but is not necessarily the case if relative orbital elements are employed):

$$\boldsymbol{r}(t) = \boldsymbol{C}(t) \cdot \boldsymbol{x}(t) \tag{2}$$

Each observation from a given set of measurements obviously satisfies:

$$\boldsymbol{u}_i \times \boldsymbol{r}(t_i) = 0, i \in [1, n] \tag{3}$$

Substituting Eq. 1 and Eq. 2 into Eq. 3 yields:

$$\boldsymbol{u}_i \times (\boldsymbol{C}(t_i)\boldsymbol{\Phi}(t_i, t_0)\boldsymbol{x}(t_0)) = 0, i \in [1, n] \tag{4}$$

It can clearly be recognized that, if $\boldsymbol{x}(t_0) = \boldsymbol{x}_0$ is solution of Eq. 4, the scaled solution $\mu\boldsymbol{x}_0$ is also a solution, leading to an infinity of solutions matching a given measurement profile. This result is known as Woffinden's dilemma.

4

2.2. Improving the Observability

Full nonobservability is however strictly valid under the aforementioned assumptions. Many authors have investigated how the observability property improves by relaxing some of them. A first possibility consists in executing maneuvers, so that the relative motion is no more homogeneous (*i.e.*, $\boldsymbol{x}(t) \neq \boldsymbol{\Phi}(t, t_0) \cdot \boldsymbol{x}(t_0)$). Examples are provided in (Woffinden and Geller, 2009b; Gaias et al., 2014; Grzymisch and Fichter, 2014a,b), where the focus is given on finding optimal location and direction of impulsive maneuvers to be performed during the rendezvous to improve the observability of the bearing-only relative navigation problem. In practice this strategy has been used to enable the vision-based activities carried out within the PRISMA mission (Noteborn et al., 2011; Delpech et al., 2012; D'Amico et al., 2013) as well as in AVANTI (Gaias and Ardaens, 2018; Ardaens and Gaias, 2018b). A second option consists in introducing a camera offset with respect to the center of mass of the spacecraft (Geller and Klein, 2014; Perez, 2017). A third approach is to improve the modeling of the relative dynamics and/or the modeling of the measurement equations to enhance maneuver-free observability. In (Lovell and Tragesser, 2004), for example, an observability criterion based on Lie derivatives for the nonlinear two-body relative problem is proposed. A beneficial effect over time is achieved by including orbit perturbations (i.e., the secular effect due to the J_2 term of the gravitational potential) in the relative motion modeling as discussed in (Gaias et al., 2014) and (Sullivan et al., 2016). This latter work also considers the eccentricity of the spacecraft orbit and nonlinearities in the measurement model. Note that these works exploit the parametrization in terms of relative orbital elements, as linearization with respect to mean orbital elements produces a better modeling of the orbit curvature compared to linearization in Cartesian coordinates.

Focusing on algorithms dedicated to IROD, Garg and Sinclair (2015) use a second-order model of the relative dynamics combined with line-of-sight measurements modeled from the Cartesian relative state; whereas Geller and Lovell (2017) alter the linear dependency of the measurement equation using cylindrical coordinates. Sullivan et al. (2016) exploit the decoupling between the weakly observable range and the observable relative geometry (see also (Gaias et al., 2014)) to define a reduced set of relative orbital elements (ROE) normalized by the relative mean longitude. The resulting normalized state vector is then used to fit the observation batch, neglecting its dynamical evolution. In order to reduce the amount of required measurements, Sullivan

5

and D'Amico (2017) propose two variants to their original algorithm. The first, fully analytical, option consists in retaining the second-order expansion of the nonlinear transformation from the mean ROE to local relative position to determine the predominant unknown scaling factor which approximates the null space of observability matrix. This approximation, in fact, allows reducing the IROD problem to a $2n$ (with n number of measurements) system of linear equations in the unknown larger scaling factor. The second option, which improves the performance of the analytical method in the presence of realistic noise, fits the scaled ROE set accounting for J_2 (secular, long-period, and short-period effects) and starting from the a-priori knowledge of the relative mean longitude derived from TLE products.

In view of the main characteristics of the scenario under considerations (*i.e.*, near-circular low Earth orbits with intersatellite distance of a few dozen kilometers), some of the aforementioned approaches are naturally excluded. Improving the observability by considering the camera offset, for example, is rather intended for close-proximity regions (*i.e.,* up to a few dozen meters) and will be unrealistic/impracticable for far-range IROD. At the same time, the methods based on an analytical model which does not include at least J_2 introduce too large modeling errors when flying in the LEO region. Although performing orbit corrections revealed a viable and practical solution for initializing angles-only relative navigation filters, this requires the estimation of additional parameters (*i.e.*, maneuver execution errors) and the expenditure of supplementary fuel during the rendezvous phase. In this framework, the proposed methodology aims at enhancing such practical solution exploiting nonlinearities in the modeling within a maneuver-free observation arc. First the decoupling between intersatellite range and shape of the relative orbit is exploited to reduce the search space of the solution. Then several least-squares fitting are performed in the vicinity of the solution of the linear model, sliding along different magnitude of the scaling factor. The obtained fitting residuals reflect the effect of the nonlinearities of the problem, thus the IROD solution corresponds to the global minimum of the fitting residuals over the scaling direction. Contrary to other works in the literature, this algorithm does not require any external a-priori information to resolve the scaling factor. The approach is detailed in the next sections. Despite its apparent simplicity, the major challenges arise when dealing with real operational conditions: the ability for the camera to distinguish the small differences with respect to the linearized relative motion, given the sensor noise, the intersatellite separation and the visibility conditions.

6

2.3. Algorithm Description

As already stated, the linear assumptions leading to the Woffinden's dilemma result in a infinity of solutions matching a given measurement profile. In reality, these approximations translate into small discrepancies which will appear when trying to fit a solution from the linear theory with a set of real measurements. Intuitively, the smallest fitting errors will be obtained in the vicinity of the true solution, allowing for a discrimination between all the collinear candidate solutions. This statement sounds simple but is in fact not obvious. A mathematical proof is provided in the Appendix to support this assertion.

In order to accurately fit the measurements, a more advanced relative motion model is required, able to faithfully capture the effects neglected by the linear model. In this case, the state propagation becomes

$$\boldsymbol{x}(t) = \boldsymbol{f}(t, \boldsymbol{x}(t_0)) \tag{5}$$

where $\boldsymbol{f}$ is a nonlinear function. Let $\boldsymbol{x}_0 = \boldsymbol{x}(t_0)$ denote the initial state vector at time t_0. The modeled relative position takes the general form $\boldsymbol{r}(t, \boldsymbol{x}_0) = \boldsymbol{g}(\boldsymbol{x}(t, \boldsymbol{x}_0))$, $\boldsymbol{g}$ also being a nonlinear function. The measurement model $\boldsymbol{h}(t, \boldsymbol{x}_0)$ is derived from the relative position:

$$\boldsymbol{h}(t, \boldsymbol{x}_0) = \frac{\boldsymbol{r}(t, \boldsymbol{x}_0)}{\|\boldsymbol{r}(t, \boldsymbol{x}_0)\|} \tag{6}$$

The problem of IROD consists in finding $\boldsymbol{x}_0$ which minimizes the loss function

$$J = \sum_{i=1}^{n} \|\boldsymbol{h}(t_i, \boldsymbol{x}_0) \times \boldsymbol{u}_i\|^2 \tag{7}$$

The difficulty here is to derive a method able to find in a reasonable time the global minimum of J. Due to the weak observability of the problem, a simple batch least-squares method will have some difficulties to converge to the global minimum. The proposed approach consists in aiding the least-squares method with the family of solutions coming from the linear theory to perform a systematical search of the best candidate within this family. For this purpose, it is first necessary to compute the linear solution. According to Eq. 4, a single measurement $\boldsymbol{u}_i$ provides a set of three equations. By combining n measurements, a set of $3n$ equations can be derived and rearranged to form the following linear system:

$$\boldsymbol{A} \cdot \boldsymbol{x}_0 = 0, \tag{8}$$

where $\boldsymbol{A}$ is a $3n \times 6$ matrix of rank 5. Due to the rank deficiency of the matrix, a non-trivial solution $\hat{\boldsymbol{x}}_0$ exists. This solution can be easily derived by computing the one-dimensional null-space of $\boldsymbol{A}$.
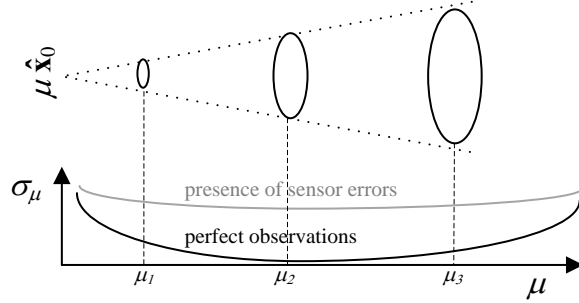

Figure 1: Fitting residuals corresponding to a series of least-squares adjustments in the vicinity of the linear solutions $\mu\hat{\boldsymbol{x}}_0$, which are schematically represented by ellipses on top of the graph.

A constrained (using an *a priori* covariance) batch least-squares adjustment is subsequently performed in the vicinity of this solution. Since $\hat{\boldsymbol{x}}_0$ is a solution in the linear theory, the batch-least squares method will easily converge to a local solution $\boldsymbol{x}_0$ in the vicinity of $\hat{\boldsymbol{x}}_0$. This process can be repeated using a scaled solution $\mu\hat{\boldsymbol{x}}_0$ (which belongs as well to the null-space of $\boldsymbol{A}$) leading to new a local solution $\boldsymbol{x}_0^\mu$. Let $\sigma(\mu)$ denote the root mean square value of the measurement fitting residuals associated to $\boldsymbol{x}_0^\mu$:

$$\sigma(\mu) = \sqrt{\frac{1}{n} \cdot \sum_{i=1}^{n} \|\boldsymbol{h}(t_i, \boldsymbol{x}_0^\mu) \times \boldsymbol{u}_i\|^2} = \sqrt{\frac{1}{n} J(\boldsymbol{x}_0^\mu)} \tag{9}$$

where $\boldsymbol{h}(t_i, \boldsymbol{x}_0^\mu)$ stands for the modeled line-of-sight measurement at time t_i corresponding to the initial relative state $\boldsymbol{x}_0^\mu$. The numerical values for the lower and upper limits of μ are derived from the physical properties of the sensor and target spacecraft: for a given measured quantity of light, it can for example be stated that the intersatellite distance must be comprised between 1 and 100 km. By varying the scaling factor μ within this range, it becomes possible to find the solution $\boldsymbol{x}_0^\mu$ which minimizes the fitting residuals σ. This process is depicted in Fig. 1, where the solution found for $\mu = \mu_2$ corresponds to the global minimum of the fitting residuals. Thanks to this approach, the search space has thus been reduced from six dimensions ($\boldsymbol{x}_0$) to only one (μ).

8

The accuracy of the solution will depend on the flatness of the valley formed by the residuals. The flatter the curve is, the less observable the problem becomes. The steepness of the curve depends on several factors which are described more in details in Section 3. One of these factors is the noise of the sensor, which tends to fade the effects of the nonlinearity, as schematically depicted in Fig. 1.

3. Numerical Analysis

3.1. Parameterization of Relative Motion

In order to ease the interpretation of the numerical analyses, it is convenient to first introduce of a set of dimensionless relative orbital elements $\delta\boldsymbol{\alpha}$ (Gaias et al., 2014):

$$\delta\boldsymbol{\alpha} = \begin{pmatrix} \delta a & \delta\lambda & \delta e_x & \delta e_y & \delta i_x & \delta i_y \end{pmatrix}^T, \tag{10}$$

where δa is the dimensionless relative semi-major axis, $\delta\lambda$ stands for the relative mean longitude, and $\delta\boldsymbol{e} = \begin{pmatrix} \delta e_x, \delta e_y \end{pmatrix}^T$ and $\delta\boldsymbol{i} = \begin{pmatrix} \delta i_x, \delta i_y \end{pmatrix}^T$ are respectively called relative eccentricity and inclination vectors.
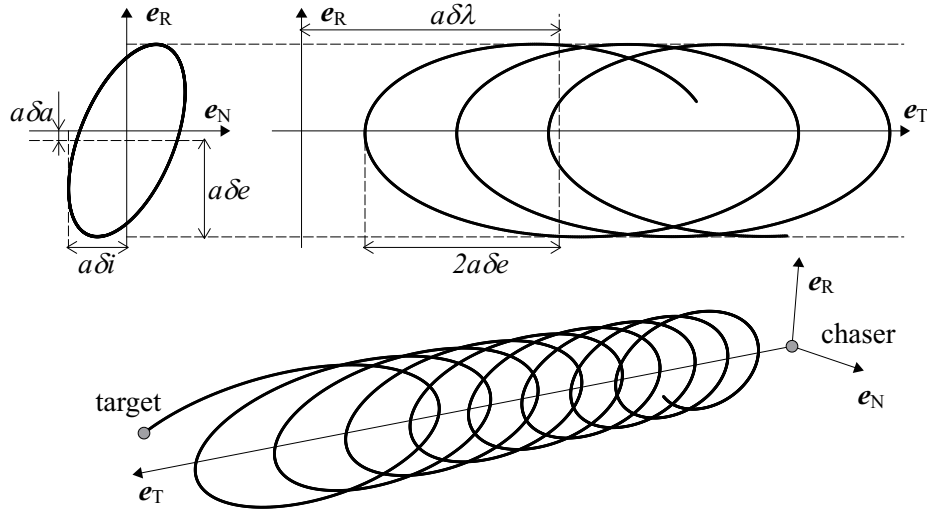

Figure 2: Relative motion parameterized with relative eccentricity/inclination vectors.

Compared to a Cartesian representation, this parameterization offers among others the advantage of providing a quick insight into the geometry of the

9

formation. Figure 2 depicts for example the relative motion in a local Cartesian orbital frame (Radial-Tangential-Normal or R-T-N), whose unit vectors are defined as follows: e_R and e_N are respectively aligned with the absolute position of the chaser and the orbit momentum, while e_T completes the triad. As depicted in Fig. 2, the size of the relative elliptical motion can be described by the means of the dimensioned (*i.e*, scaled with the semi-major axis a) relative orbital elements.

This set of relative orbital elements is also particularly suited to the problem of angles-only navigation, because the weakly observable intersatellite distance almost coincides with one component, yielding a geometrical decoupling between size and range of the relative motion. In fact, in the case of a rendezvous with two spacecraft separated by several dozen kilometers, the apparent motion seen by the camera mainly corresponds to the eclipse described in the (Radial-Normal), while $a\delta\lambda$ describes the mean along-track separation. For clarity, this parameterization will from now on always be used to describe the relative motion.

3.2. Relative Motion and Measurement Models

As already stated, accurate models for the relative motion and measurements are needed to enable the observation of small differences with respect to the linear motion model. Two options are investigated:

- **Numerical propagation**. In this case, x is the Cartesian inertial relative state vector, g is the identity and f corresponds to a numerical integration of the equations of motion considering a gravity field which includes at least J_2. As the equations are numerically integrated, no linearization is performed and the overall accuracy depends on the order and degree of the considered terms of the gravitational potential, as well as on the additional perturbations included in the model (*e.g.*, aerodynamical drag, solar radiation pressure, third-body). This model is very accurate, provided that these perturbations can be precisely modeled, which is in reality often not the case, given the uncertainties associated to the atmosphere density and to the characteristics of a noncooperative target. The main drawback of this model lies in the high computational costs.

- **Analytical propagation using mean relative orbital elements**. In this case, the relative motion model is parameterized using the mean

10

relative orbital elements (*i.e.*, $\boldsymbol{x} = \delta\boldsymbol{\alpha}$) introduced in Section 3.1, for which a linear motion model is available (*i.e.* $\delta\boldsymbol{\alpha}(t) = \boldsymbol{\Phi}(t, t_0) \cdot \delta\boldsymbol{\alpha}(t_0)$, see Gaias et al. (2015)). On the contrary, the model of the relative position $\boldsymbol{g}$ is not linear anymore. In order to retrieve the Cartesian relative position, it is first necessary to convert the mean relative orbital elements into osculating relative elements, thus recovering long-term and short-term contributions induced by J_2, then to map the osculating elements into a Cartesian position vector. This model allows the introduction of additional empirical parameters, in order to reflect the mean effect of the differential drag. However, it does not include for the moment the higher terms of the gravity field and is thus slightly less accurate than the numerical integration with a full gravity field, but presents the advantage of being computationally-light.

As rule of thumb, it can be stated that the method will correctly perform if the measurement noise is similar to the errors of the model but smaller than the discrepancies between the model and the linear motion model (otherwise they cannot be observed). The camera (Jørgensen et al., 2003) employed for ARGON and AVANTI exhibits a line-of-sight noise of about 40" at far-range (corresponding to less than half-a-pixel). This translates into an error of about 5 m at 30 km. The differential drag is the second largest perturbation after J_2 in low Earth orbit. This perturbation can be helpful to accentuate the discrepancies with respect to the linear motion model but is extremely difficult to faithfully model, especially when dealing with a noncooperative target, with unknown geometry and attitude. Hence, in the case of IROD, it might be more judicious to reduce the observation time span as much as possible (a few orbits), in order to limit the effect of this mismodeled perturbation.

Fig. 3 depicts the performance of the different models, which has been assessed using a reference relative motion coming from the PRISMA mission (in a phase when the spacecraft were separated by 30 km). This reference relative trajectory has been determined using differential GPS and is accurate at the subcentimeter level (Ardaens et al., 2012). The initial conditions for each model have been adjusted to best fit the reference trajectory, as typically done in an orbit determination task. The model of Fig. 3a consists in a numerical propagation using a 20x20 gravity field and including the perturbation due to the drag (using simple cannon-ball model and empirically-measured ballistic coefficients), the solar radiation pressure and
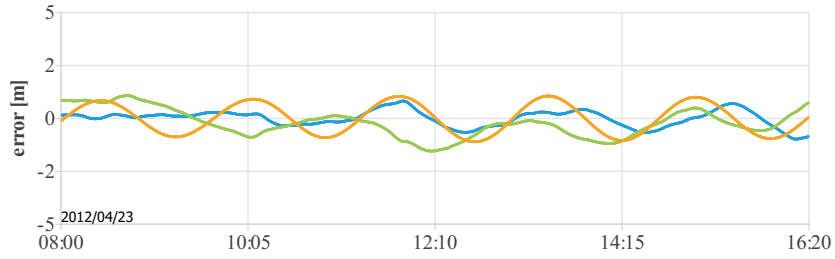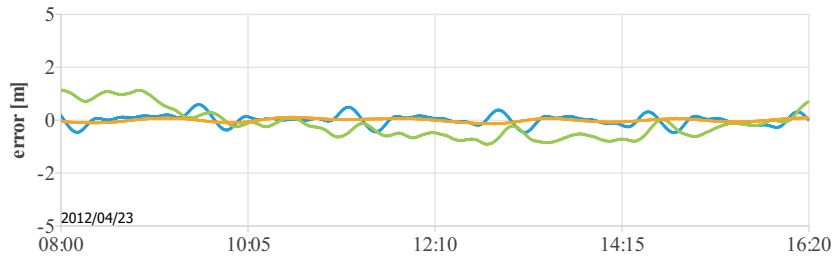
11
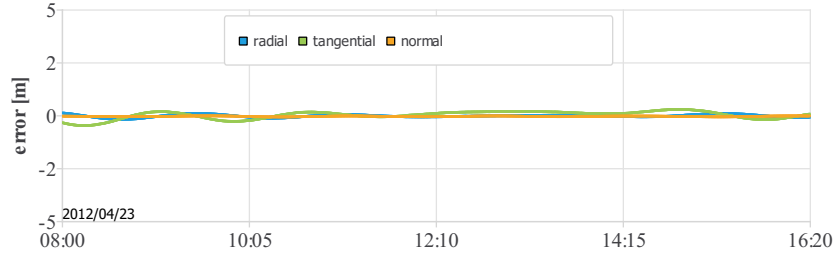
(a) Numerical propagation including all perturbations.
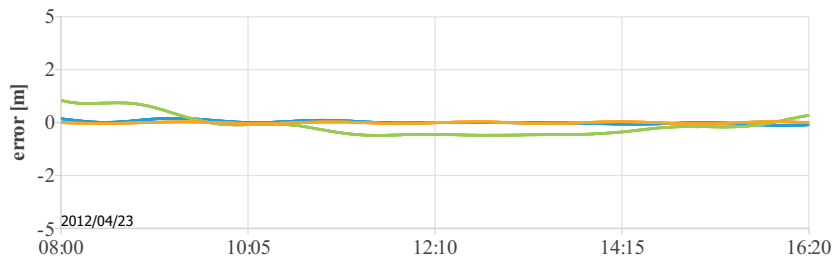
(b) Numerical propagation including only a full gravity field.

(c) Numerical propagation including only J_2.

(d) Analytical propagation of relative orbital elements.

Figure 3: Error of different relative motion models with respect to GPS-based relative orbit determination from the PRISMA mission.

the luni-solar perturbations. This model performs well but can hardly be used during noncooperative operations, since the drag coefficients need to be empirically determined to reach a good modeling of the differential drag. This was possible with the PRISMA spacecraft, both equipped with GPS receiver, but is much more arduous in the case of a noncooperative target. The models of Fig. 3b and Fig. 3c are numerical propagations respectively considering a 20x20 gravity field and only J_2. The model corresponding to Fig. 3d is the analytical propagation using relative orbital elements. Note that the model using the 20x20 gravity field slightly outperforms the J_2-numerical propagation and the analytical model, but these two models are still accurate at the meter level. In order to better compare these errors with the observation noise, Fig. 4 depicts the line-of-sight errors resulting from the model errors. This figure indicates that, for a limited time span of 5 orbits, all model errors stay well below the sensor noise. As a result, it can be stated that both analytical and numerical models are suited for IROD.
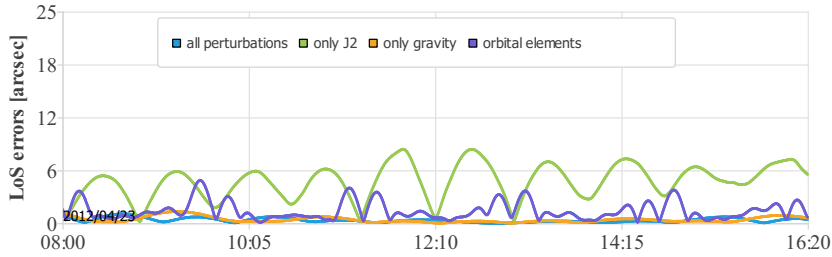

Figure 4: Line-of-sight (LoS) errors introduced by the model deficiencies.

3.3. Influence of different factors

As already stated in Section 2.3, several effects contribute to influence the steepness of the valley of fitting residuals. This section intends to investigate the impact of five factors by the means of simulations. The ultimate validation with flight data will follow in the next section. The scenario used for the simulation is directly inspired from the ARGON experiment. A chaser satellite is flying on a 750 km high, dusk-dawn, Sun-synchronous, near-circular orbit and observes a target satellite at 30 km distance. The formation configuration is defined by $a\delta\boldsymbol{\alpha} = \begin{pmatrix} -20 & -30000 & -50 & -390 & 0 & 295 \end{pmatrix}$ m. For the need of the simulations, the reference motions of the chaser and target are numerically propagated using a 20x20 gravity field, and including the third-body, solar radiation pressure and drag perturbation. The default

13

settings for the different scenarios foresee perfect line-of-sight measurements and a maneuver-free observation arc of two orbits (these parameters will be modified case by case if needed). A set of observations is finally created from the simulated states of the chaser and target spacecraft.

The investigations are performed by the means of residuals plots (*cf.* Fig. 1) created according to the method described in Section 2.3. To that end, the linear solution is first derived by building the system $\boldsymbol{A} \cdot \boldsymbol{x}_0 = 0$ (*cf.* Eq. 4). Since relative orbital elements are used, care has to be taken to define the matrix $\boldsymbol{C}$, which maps the relative orbital elements into a Cartesian relative position (Gaias et al., 2014):

$$\boldsymbol{C}(t) = \begin{pmatrix} 1 & 0 & -\cos u(t) & -\sin u(t) & 0 & 0 \\ 0 & 1 & 2\sin u(t) & -2\cos u(t) & 0 & 0 \\ 0 & 0 & 0 & 0 & \sin u(t) & -\cos u(t) \end{pmatrix}, \quad (11)$$

where u stands for the mean argument of latitude and i for the inclination. Note that this linear measurement model is not very accurate but is sufficient to derive a coarse solution to initialize the relative orbit determination. Since $\delta\lambda$ is not observable (Gaias et al., 2014), the linear solution corresponding to a specific value $a\delta\lambda = L$ in a least-squares sense can be derived as follows:

$$\tilde{\boldsymbol{A}} = \begin{pmatrix} \boldsymbol{A}_1 & \boldsymbol{A}_3 & \boldsymbol{A}_4 & \boldsymbol{A}_5 & \boldsymbol{A}_6 \end{pmatrix} \quad (12a)$$

$$\boldsymbol{b} = -L \cdot \boldsymbol{A}_2 \quad (12b)$$

$$\boldsymbol{\gamma} = (\tilde{\boldsymbol{A}}^T \cdot \tilde{\boldsymbol{A}})^{-1} \cdot \tilde{\boldsymbol{A}}^T \cdot \boldsymbol{b} \quad (12c)$$

where $\boldsymbol{A}_i$ corresponds to the ith column of $\boldsymbol{A}$. Finally, the linear solution $\hat{\boldsymbol{x}}_0^L$ corresponding to the relative motion at mean relative longitude L is reconstructed as

$$\hat{\boldsymbol{x}}_0^L = \begin{pmatrix} \gamma_1 & L & \gamma_2 & \gamma_3 & \gamma_4 & \gamma_5 \end{pmatrix}, \quad (13)$$

where γ_i represents the ith component of $\boldsymbol{\gamma}$.

In order to create the residual plots, a granularity of 1 km is employed, which means that the linear solution $\hat{\boldsymbol{x}}_0^L$ corresponding to the relative motion at discretized distance $L \in [\![5, 100]\!]$ km is used to initialize the batch least-squares adjustments. This process is executed 95 times, starting with $L=5$ km. The covariance matrix used to constrain the solution is set as

14

$\boldsymbol{P} = \mathrm{diag}(100^2, 1^2, 100^2, 100^2, 100^2, 100^2)$ m^2. Based on the residual plots, the influence of several factors can be investigated:

- **Observation time span**. A longer observation time span increases the impact of the nonlinearities and perturbations and thus plays a predominant role in the improvement of the solution accuracy. Fig-
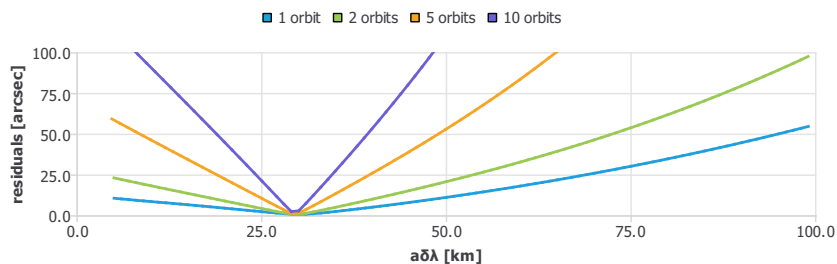

Figure 5: Improvement of observability due to the observation time span.

ure 5 shows that a significant steepness already appears by collecting observations over more than 2 orbits.

- **Execution of maneuvers**. Maneuvers act as perturbations which introduce additional discrepancies with respect to the linear motion. Even if any maneuver could in principle be used, the main drivers during a rendezvous concern the mission safety and propellant consumption. For IROD, it is tempting to seek for the smallest maneuver able to improve observability given the intersatellite satellite separation and the sensor noise. Since the drift of the formation is unknown at this stage, it is preferable to execute cross-track maneuvers which will not put the formation at a risk.

In order to investigate their impact on the IROD, cross-track maneuvers of different sizes are executed. Their locations do not influence the results, thus each maneuver has simply been executed 100 minutes after the simulation start. What counts is their magnitude, which is directly related to the amount of nonhomogeneity introduced in the relative motion model. Figure 6 indicates that, at 30 km separation, a 3 cm/s maneuver can already greatly improve the steepness of the residual curve. Note that a known and predicable perturbation (for example solar radiation pressure or differential drag) will have a same effect, as long as it can be accurately modeled.
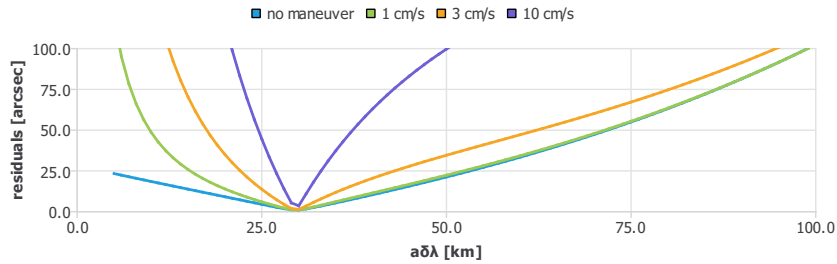
15

Figure 6: Improvement due to the execution of cross-track maneuvers.

- **Sensor noise**. The noise of the line-of-sight measurements contributes to flatten the curve, and is thus the biggest challenge for the IROD. Figure 7 depicts the effect of the observation noise. It can be noticed
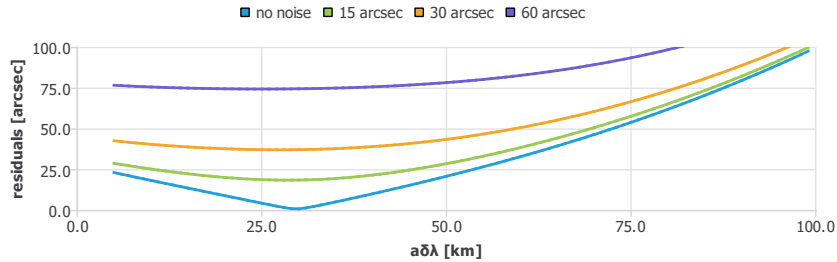

Figure 7: Negative influence of sensor noise.

that a small noise level of 15" already causes a significant flattening of the curve, diluting thus the accuracy of the solution. During a rendezvous, the noise will depend on the camera characteristics but also on the size of the imaged target (thus on the separation and target characteristics). As rule of thumb, the noise decreases when the image of the target increases, since the centroiding function in charge of measuring the position of the center of mass is more precise when the image is spread over more pixels (this is not true anymore at mid-range where the image of the target cannot be considered anymore as a point spread function, *cf.* Ardaens and Gaias (2018b)). In case of larger measurement noise, it will be necessary to increase the observation time span to counterbalance the flattening effect introduced by the sensor noise.

- **Visibility**. ARGON was a favorable case, because the relative motion

16

was fully visible thanks to the dusk-dawn orbit of the PRISMA satellites. When flying on an arbitrary orbit in LEO, part of the motion is not visible anymore, because the target is eclipsed or because the camera is blinded by the Sun. The AVANTI experiment showed that as little as 10% of the relative motion was visible during the rendezvous (Ardaens and Gaias, 2018a). This has as well a strong impact in the shape of the residuals as depicted in Fig. 8.
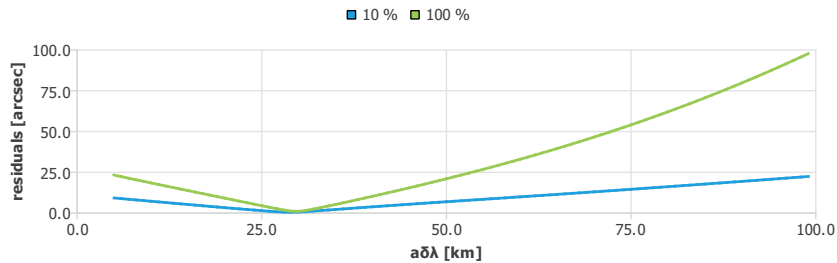

Figure 8: Influence of the visibility of the relative motion.

In order to simulate this case, only the measurements taken at mean argument of latitude $u \in [0, 2\pi/10]$ are kept. In Fig. 8, the small level of residuals at wrong separations (*e.g.*, at 100 km) can be explained by the fact that the least-squares process will simply find a wrong solution which will correspond to the very few available measurements, thus exhibiting good fitting residuals. Here again, increasing the observation time span or executing maneuvers can help mitigating this problem.

- **Formation configuration**. The configuration of the formation also plays a role in the overall observability. It would be out of the scope of the paper to investigate all the possible configurations. For the sake of this analysis, only $\delta\lambda$ is changed, keeping the other relative orbital elements constant. Such assumption does not represent a limitation in the validity of the analysis, but rather reflects the fact that a slowly drifting (anti-)parallel e/i configuration trajectory is the operationally safest way to rendezvous a noncooperative target. Figure 9 shows that, when staying in the same order of magnitude of several dozen kilometers, the increasing separation slightly flattens the curve, but this effect is not as pronounced as the ones described above.
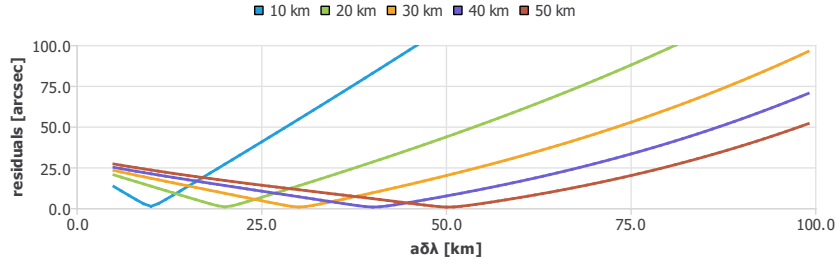
17

Figure 9: Influence of the intersatellite separation.

4. Flight Demonstration

4.1. Selection of the Demonstration Cases

The demonstration cases presented in this section aim at validating the method described above with flight data from the ARGON and AVANTI experiments. Unfortunately, very few data arcs could be exploited. The ARGON experiment was short (4 days) with frequent maneuvers and several data outages due to the limited onboard data storage capability. As a result, only two representative maneuver-free data arcs could be extracted. The AVANTI experiment was much longer (more than 2 months of observations) and offers numerous interesting data arcs to exercise IROD. However, it suffers from the fact that no reference exists for the relative state (since the target spacecraft was fully noncooperative) except for one single occasion. During this particular day, a ground-based radar-tracking campaign has been conducted to precisely measure the relative state of the formation (Ardaens and Gaias, 2018a). Consequently, it was possible to extract a single demonstration case from the AVANTI experiment for which an external reference is available.

4.2. 5h-Long Arc with Optimal Visibility (ARGON)

The IROD is performed using a 5h-long (or 3 orbits) maneuver-free data arc on April 24th, 2012. At that time the chaser and target are separated by 30 km. The two models described in Section 3.2 are investigated to create the residuals plots in Fig. 10 and represented by two different colors. The solution to the IROD corresponds to the measurement fitting which exhibits the smallest residuals. This global minimum is graphically identified by a round marker of the same color as the corresponding curve.
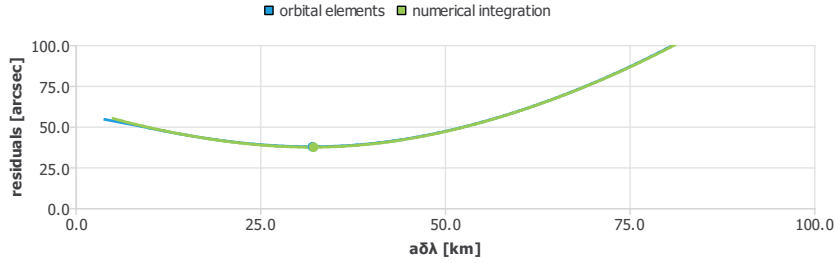
18

Figure 10: Solution for the ARGON case.

Table 1 summarizes the solutions found using both models, as well as the reference relative state derived with relative GPS. Table 1 indicates that both models exhibit similar performance, reaching accuracy of a few percents. However the numerical model comes at the cost of much larger computational time. On a desktop computer equipped with a Core i5 processor clock at 2.6 GHz, a few dozen seconds are typically required to derive the solution based on the analytical model while the numerical integration can take more than one hour, depending on the number of measurements and iterations required for the least-squares adjustments.

Reference	[-21 -29568 -51 -395 -4 295] m
Relative orbital elements	[-20 -32000 -55 -429 -4 317] m
Numerical propagation	[-21 -32146 -56 -430 -4 319] m

Table 1: Solution $\delta\boldsymbol{\alpha}$ for the 5h-long ARGON case.

The similarity of the results can be explained by the fact that both models are more or less equivalent in this case. The differential drag at the altitude of PRISMA (750 km) is weak and the short observation time limits as well its effects. In both cases, the longitudinal (along-track) accuracy of the solution is equivalent to the one of TLEs (a few km). The lateral (radial + cross-track) accuracy outperforms the TLEs by several orders of magnitude (it is indeed not uncommon for TLEs to exhibit cross-track errors of a few hundred meters (Kahle et al., 2014)). For completeness, the observation residuals (parameterized in terms of right-ascension α and declination δ) corresponding the selected solution are depicted in Fig. 11. It can be seen that, thanks to the dusk-dawn orbit of the PRISMA satellites, the measurements are homogeneously distributed over time.

19

Figure 11: Residuals of the orbit determination corresponding to the solution for the 5h-long ARGON case.

4.3. 14h-Long Arc with Optimal Visibility (ARGON)

If more time is available to collect measurements, it might be judicious to extend the observation arc to improve the observability (as depicted in Fig. 5). The second study case comes again from the PRISMA mission, but spans now 14 h (April 25th 2012, from 2:00 to 14:00 UTC). At that time, the chaser and target are separated by 23.5 km.
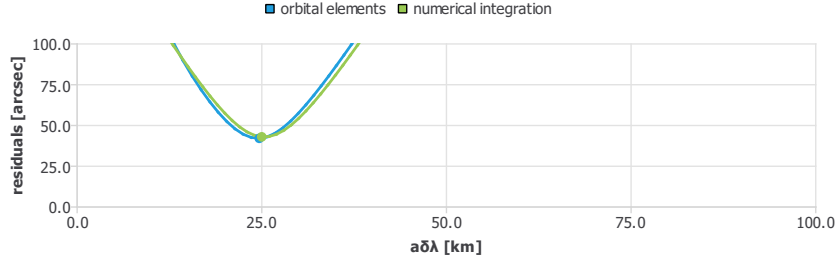
Figure 12: Solution for the ARGON case.

As depicted in Fig. 13, a large data gap (7 hours) affects the observations, but this is not an issue as long as the measurements are located at the beginning and at the end of the data arc.

Reference	[-131 -23650 -20 -303 -4 247] m
Relative orbital elements	[-139 -24593 -21 -315 -5 257] m
Numerical propagation	[-139 -24990 -19 -321 -5 261] m

Table 2: Solution $\delta\boldsymbol{\alpha}$ for the 14h-long ARGON case.

20

As expected, Figure 12 shows that the steepness of the residual curve is much more pronounced, leading to a more accurate solution. Table 2 indicates that the range ambiguity can be determined with an error of less than 5%. In such a case, the result from the IROD clearly outperforms a solution derived from TLEs.
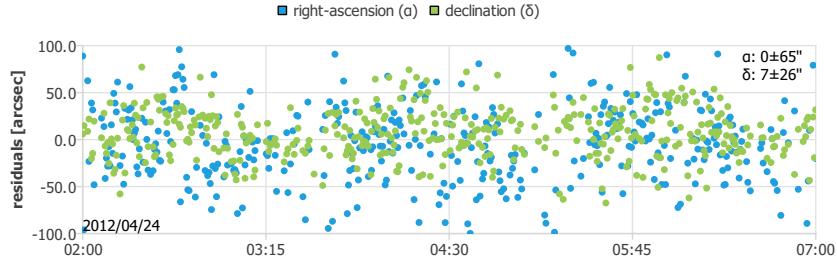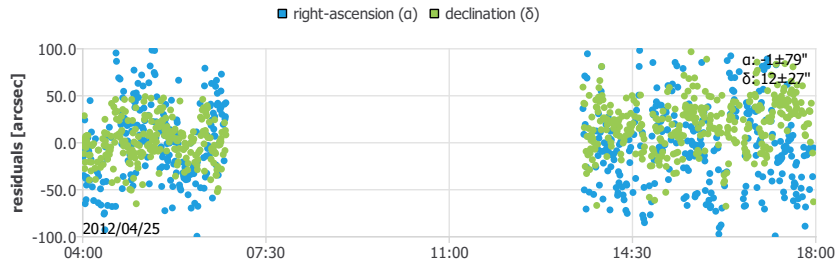

Figure 13: Residuals of the orbit determination corresponding to the solution for the 14h-long ARGON case.

4.4. 18h-Long Arc with Poor Visibility (AVANTI)

The same method is now applied to a data arc coming from the AVANTI experiment. The collection of observations starts on October 20th, 2016 22:00 UTC when the satellites are separated by 45 km. Due to the poor visibility conditions encountered during AVANTI, this case is much more challenging because only 10 minutes of observations are available every orbit. According to the preliminary investigations done in Section 3.3, the residual curve is expected to be extremely flat due to the limited visibility (*cf.* Fig. 8) and to the larger distance (*cf.* Fig. 9). In order to counterbalance this flatness, it is necessary to extend the observation time span: the data arc has thus been extended to span 18 h (11 orbits). Figure 14 depicts the residual plot obtained using the numerical and analytical models.

In view of the difficulty to estimate the drag of a noncooperative object, this perturbation has been first disabled in the numerical model. Both models exibit a very similar residual curve. However, its extrem flateness makes the accurate determination of the global minimum very challenging: a difference of 10% can be observed in Table 3 between both solutions. The reference solution is derived from the ground-based radar observations and is expected to be accurate to 10 m.

21
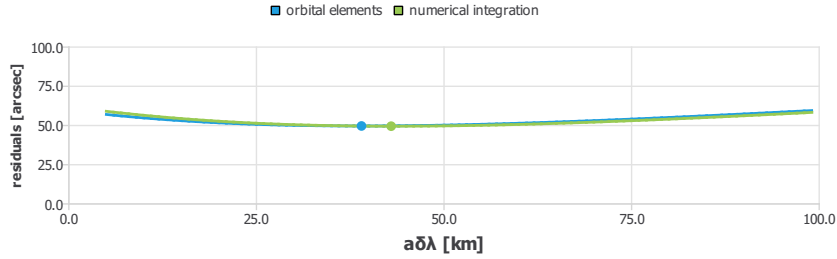
Figure 14: Solution for the AVANTI case.

Reference	[84 44786 155 609 -8 714] m
Relative orbital elements	[68 39000 137 533 -10 625] m
Numerical propagation (no drag)	[78 43953 152 614 -12 704] m
Numerical propagation (with drag)	[89 48947 164 696 -14 782] m

Table 3: Solution $\delta\boldsymbol{\alpha}$ for the AVANTI case.

It can be tempting to include the perturbation due to the differential drag to improve the observability. Since a reference trajectory is available for the target, it is possible to estimate empirically the drag coefficient of the target.
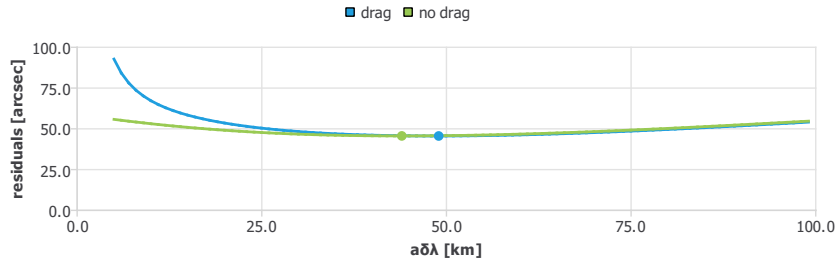
Figure 15: Solution found by enabling and desabling the drag.

Figure 15 depicts the results obtained by including the drag. As expected, the residual curve is steeper when considering this perturbation but the improvement is unfortunately too weak at this intersatellite distance to really enhance the accuracy of the solution. In fact, Table 3 indicates that the solution found by activating the differential drag is even less accurate.

The orbit determination residuals are finally depicted in Fig. 16, highlighting the challenging sparsity of the measurement distribution.

22
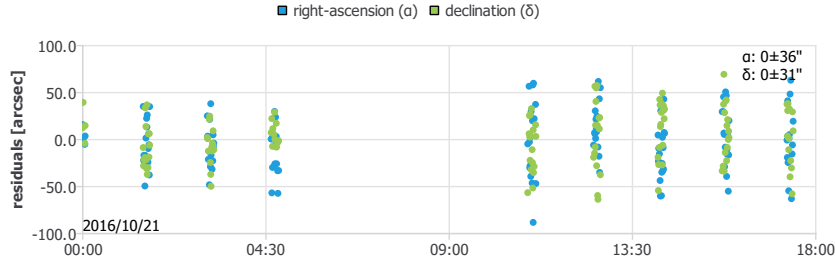
Figure 16: Residuals of the orbit determination corresponding to the solution for the AVANTI case.

Conclusion

Despite the weak observability of the angles-only relative navigation problem, it is possible to perform an initial relative orbit determination in low Earth near-circular orbit without executing any maneuver, by simply observing during a few orbits the apparent motion of a target with a camera.

The proposed approach aims at exploiting the small discrepancies which can be observed between a linear relative motion and the reality. The method consists in performing a series of least-squares adjustments at varying distances in the vicinity of a family of collinear solutions coming from the linear theory. The solution of the problem is found by selecting the distance corresponding to the global minimum of the fitting residuals. It order to correctly perform, this method relies on relative motion models which can effectively capture these small differences. Two models are considered: an analytical model based on relative orbital elements which considers only J_2 and a numerical propagation for which additional perturbations can be included. De facto the proposed method consists in an oriented search in the solution space, where the search direction is determined by varying the relative range, which corresponds to one component of the state expressed in terms of relative orbital elements (*i.e.*, the relative mean longitude). Accordingly, this method does not have the elegance of a direct analytical solution and is computationally intensive. However the use of an analytical model can reduce the computational time by two orders of magnitude without degradation of performance, making this method eligible for onboard implementation.

Different factors influence the accuracy of the solution, such as observation time span, visibility conditions, formation configuration, presence of additional maneuvers, and sensor noise. Consequently, it is difficult to out-

23

line a general performance index of the proposed methodology. Nevertheless its effectiveness has been proved by processing two different real-data sets coming from the ARGON and AVANTI experiments. The obtained results show that this approach can at least achieve the same accuracy as offered by Two-Line-Element products.

Acknowledgments

Appendix

The proposed algorithm relies on the fact that the residual curve $\sigma(\mu)$ is convex and reaches its minimum for $\mu = \hat{\mu}$, where $\hat{\mu}$ is the value corresponding to the solution yielding the global minimum of the loss function J. Unfortunately this behavior is not always true for an arbitrary loss function $J(\boldsymbol{x})$ (for example if J depends on $\cos^2 \mu$). Thus, the empirically observed convexity of the residual function has to be linked to the nature of the problem under consideration. For simplicity, the minimum $m(\mu)$ of the loss function J will be now investigated instead of the residual curve $\sigma(\mu)$ (this is justified by the fact that m is convex if and only if σ is convex, cf. Eq. 9).

In order to analyze the behavior of this minimum, an analytical formulation of the problem is required. Unfortunately, the minimum $m(\mu)$ is the result of an iterative nonlinear least-squares estimation and cannot be analytically described. Thus the problem needs to be simplified and reshaped to reach a formulation for which an analytical expression of the minimum can be found.

Until now, it has been stated that the nonlinearities with respect to Eq. 4 were responsible for the weak observability. This is correct but it is possible to be more precise. In fact, it has to be distinguished if the nonlinearities are due to:

1. the first order linearization done when deriving the relative motion model;
2. the neglect of the curvature of the orbital path.

These effects can be isolated and thus individually quantified by adopting a specific parameterization of the relative state $\boldsymbol{x}$. In fact, the curvature of the orbital path can be taken into account by using a set of relative orbital elements or a set of curvilinear Cartesian components to describe the vector $\boldsymbol{x}$. In this case, the relative motion model $\boldsymbol{f}$ describes the time evolution of the state vector (and thus deals with the possible approximations due to the linearization of the relative motion model) while the function $\boldsymbol{g}$ maps the relative state vector $\boldsymbol{x}$ into a rectilinear Cartesian relative position, thus capturing the effect of the curved orbital path.

A linear model describing the time evolution of the curvilinear Cartesian relative state vector is now adopted. As seen later, compared to a parameterization based on relative orbital elements such as the one described in Section 3.1, this choice is driven by the fact that a simpler $\boldsymbol{g}$ function is subsequently obtained. An alternative precise linear model using a curvilinear Cartesian state is thus needed for the sake of the demonstration. Two options are now investigated: the curvilinear Hill-Clohessy-Wiltshire (HCW) (de Bruijn et al., 2011) and Gim-Alfriend (Gim and Alfriend, 2003) models. The latter is in fact based on relative orbital elements but provides a linear mapping $\boldsymbol{T}$ to transform the orbital elements into a curvilinear Cartesian state representation (that is, $\boldsymbol{x}(t) = \boldsymbol{T}(t)\boldsymbol{D}(t)\boldsymbol{\varphi}(t,t_0)\boldsymbol{D}^{-1}(t_0)\boldsymbol{T}^{-1}(t_0)\boldsymbol{x_0} = \boldsymbol{\Phi}(t,t_0)\boldsymbol{x_0}$, $\boldsymbol{\varphi}$ being the state transition matrix based on mean relative orbital elements and $\boldsymbol{D}$ the transformation matrix between mean and osculating elements). Note that, in near-circular orbits, $\boldsymbol{\varphi}$ is equivalent to the state transition matrix of the model described in Section 3.1. The benefits of the Gim-Alfriend formulation in terms of accuracy lies in the mapping matrix $\boldsymbol{T}$, which is more accurate than the matrix $\boldsymbol{C}$ described by Eq. 11.
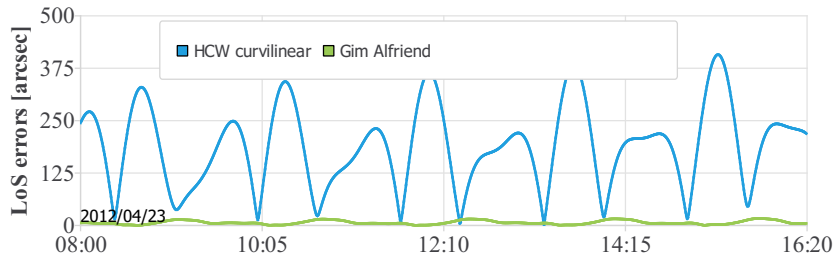

Figure 17: Line-of-sight (LoS) errors introduced by the model deficiencies.

In order to quantify the nonlinearities neglected by the linear motion models, the same approach used to create Fig. 4 is employed: both models are

25

fitted against an accurate nonlinear reference model and the difference in terms of line-of-sight errors is analyzed. Figure 17 shows that the angular errors introduced by the curvilinear HCW model are large despite the modeling of the curvature of the orbital path. This is due to the fact that this simple model does not take the effect of J_2 into account, thus resulting in unacceptable errors. Obviously this model is not adapted to our problem. On the contrary, the Gim-Alfriend model behaves much better, because it includes in the state transition matrix a linear model for the effect of J_2. Using this model, the line-of-sight errors introduced by the model deficiencies over several orbits are below the sensor noise and thus cannot be observed (that is, it does not make any observable difference to use a state transition matrix $\boldsymbol{\Phi}$ instead of a nonlinear model $\boldsymbol{f}$ to describe the time evolution of the relative state vector $\boldsymbol{x}$). The Gim-Alfriend model deficiencies can thus be treated together with the sensor noise. Consequently, it can be assumed that it is mainly the curvature of the orbital path which brings observability and which is measured by the relative orbit determination.

Using a linear relative motion model, the general nonlinear measurement equation described by Eq. 3:

$$\boldsymbol{u}_i \times \boldsymbol{r}(t_i) = \boldsymbol{u}_i \times (\boldsymbol{g}(t_i, \boldsymbol{f}(t_i, \boldsymbol{x}_0)) = 0, i \in [1, n] \tag{14}$$

can be simplified to:

$$\boldsymbol{u}_i \times (\boldsymbol{g}(t_i, \boldsymbol{\Phi}(t_i, t_0)\boldsymbol{x}_0)) = 0, i \in [1, n] \tag{15}$$

It is now assumed that the curvilinear relative state is expressed in the orbital frame and that the components are ordered in the Radial-Tangential-Normal sequence. For the rendezvous problem under consideration (that is, the relative motion is mainly an along-track separation), the rectilinear relative position $\boldsymbol{r}$ can be approximated from the curvilinear relative position $\boldsymbol{\breve{r}}$ as:

$$\boldsymbol{r} = \boldsymbol{\breve{r}} + \begin{pmatrix} R - \sqrt{R^2 + \breve{r}_2^2} \\ 0 \\ 0 \end{pmatrix} \tag{16}$$

where R is the radius of the circular orbit and $\breve{r}_2$ denotes the along-track component of the relative position. Noting that $R \gg \breve{r}_2$, this simplifies to:

$$\boldsymbol{r} = \boldsymbol{\breve{r}} + \begin{pmatrix} -\frac{\breve{r}_2^2}{2R} \\ 0 \\ 0 \end{pmatrix} \tag{17}$$

26

Let the state transition matrix be split into two blocks such as $\boldsymbol{\Phi} = \begin{pmatrix} \boldsymbol{\Phi}_{\text{1-3,1-6}} \\ \boldsymbol{\Phi}_{\text{4-6,1-6}} \end{pmatrix}$ and let $\boldsymbol{\Phi}_{\text{2,1-6}}$ denote the second line of the matrix $\boldsymbol{\Phi}$. Noting that $\breve{\boldsymbol{r}} = \boldsymbol{g}(\boldsymbol{x}) = \boldsymbol{g}(\boldsymbol{\Phi}\boldsymbol{x}_0) = \boldsymbol{\Phi}_{\text{1-3,1-6}}\boldsymbol{x}_0$, Eq. 15 takes the form

$$\boldsymbol{u}_i \times \left(\boldsymbol{\Phi}_{\text{1-3,1-6}}\boldsymbol{x}_0 - \frac{1}{2R} \begin{pmatrix} 1 \\ 0 \\ 0 \end{pmatrix} \boldsymbol{x}_0^T \boldsymbol{\Phi}_{\text{2,1-6}}^T \boldsymbol{\Phi}_{\text{2,1-6}}\boldsymbol{x}_0 \right) = 0, i \in [1, n] \qquad (18)$$

Thus, with respect to the general nonlinear formulation of Eq. 14, the problem has been simplified to the minimization of a quadratic function, which seems simpler but is in fact still not obvious. The quadratic part $\boldsymbol{q}$, corresponding to the model of the curvature of the orbital path, is now introduced for simplification:

$$\boldsymbol{q}(\boldsymbol{x}) = -\frac{1}{2R} \begin{pmatrix} 1 \\ 0 \\ 0 \end{pmatrix} \boldsymbol{x}^T \boldsymbol{\Phi}_{\text{2,1-6}}^T \boldsymbol{\Phi}_{\text{2,1-6}}\boldsymbol{x} \qquad (19)$$

The algorithm described in Section 2.3 consists in fixing one component of the state vector to a parameter μ, in order to reduce the dimension of the search space. Let $\hat{\boldsymbol{x}}_0^\mu$ denote the linear solution (*i.e.*, found by neglecting the curvature of the orbital path) for a given μ. This solution is easily computed as shown in Section 3.3. A more general formulation is recalled here for completeness. The initial state vector $\boldsymbol{x}_0$ is parameterized as $\boldsymbol{x}_0 = (\tilde{\boldsymbol{x}}_0, \mu)$ for simplicity. Without loss of generality and to simplify the notation, the parameter μ is arbitrarily chosen to be the last component (as seen earlier in the paper, it is in reality more convenient to chose the second component corresponding to the along-track relative position, because a physical range for this variable can be more intuitively derived). Starting from Eq. 18 and neglecting the quadratic part, an approximate relation is obtained:

$$\boldsymbol{u}_i \times (\boldsymbol{\Phi}_{\text{1-3,1-6}} \cdot \boldsymbol{x}_0) = 0, i \in [1, n] \qquad (20)$$

which expands to:

$$\boldsymbol{u}_i \times (\boldsymbol{\Phi}_{\text{1-3,1-5}} \cdot \tilde{\boldsymbol{x}}_0) = -\mu \boldsymbol{u}_i \times \boldsymbol{\Phi}_{\text{1-3,6}}, i \in [1, n] \qquad (21)$$

where $\boldsymbol{\Phi}_{\text{1-3,1-6}} = \begin{pmatrix} \boldsymbol{\Phi}_{\text{1-3,1-5}} & \boldsymbol{\Phi}_{\text{1-3,6}} \end{pmatrix}$ has been split into the blocks. After accumulating n measurements, a linear system is obtained (identified by the subscript $\square_{\text{L}}$ which denote the linear problem):

$$\boldsymbol{A}_{\text{L}}\tilde{\boldsymbol{x}}_0 = \mu \boldsymbol{b}_{\text{L}} \qquad (22)$$

27

whose 5-dimensional solution is given in a least-squares sense by:

$$\hat{\tilde{\boldsymbol{x}}}_0^\mu = \mu(\boldsymbol{A}_{\mathrm{L}}^T\boldsymbol{A}_{\mathrm{L}})^{-1}\boldsymbol{A}_{\mathrm{L}}^T\boldsymbol{b}_{\mathrm{L}} = \mu\boldsymbol{A}_{\mathrm{L}}^+\boldsymbol{b}_{\mathrm{L}} \tag{23}$$

Here the Moore–Penrose pseudoinverse $\boldsymbol{A}^+ = (\boldsymbol{A}^T\boldsymbol{A})^{-1}\boldsymbol{A}^T$ is used to simplify the notation. Thus, the 6-dimensional linear solution $\hat{\boldsymbol{x}}_0^\mu$ is a function of μ.

In the algorithm described in Section 2.3, a series of local minimizations is done in the vicinity of the solution $\hat{\boldsymbol{x}}_0^\mu$. Thus, it is legitimate to assume that the solution of each minimization will be close to $\hat{\boldsymbol{x}}_0^\mu$. By linearizing Eq. 18 around this linear solution, the following relation is obtained.

$$\boldsymbol{u}_i \times \left(\boldsymbol{\Phi}_{1\text{-}3,1\text{-}6}\boldsymbol{x}_0 + \boldsymbol{q}(\hat{\boldsymbol{x}}_0^\mu) + \left.\frac{d\boldsymbol{q}}{d\boldsymbol{x}_0}\right|_{\boldsymbol{x}_0=\hat{\boldsymbol{x}}_0^\mu}(\boldsymbol{x}_0 - \hat{\boldsymbol{x}}_0^\mu) \right) = \tag{24}$$

$$\boldsymbol{u}_i \times \left(\boldsymbol{\Phi}_{1\text{-}3,1\text{-}6}\boldsymbol{x}_0 - \frac{1}{2R}\begin{pmatrix}1\\0\\0\end{pmatrix}\hat{\boldsymbol{x}}_0^{\mu T}\boldsymbol{\Phi}_{2,1\text{-}6}^T\boldsymbol{\Phi}_{2,1\text{-}6}(2\boldsymbol{x}_0 - \hat{\boldsymbol{x}}_0^\mu) \right) = 0, i \in [1,n] \tag{25}$$

The same approach used for Eq. 21 is now used to restrict the problem in a 5-dimensional space:

$$\boldsymbol{u}_i \times \left(\boldsymbol{\Phi}_{1\text{-}3,1\text{-}5} - \frac{1}{R}\begin{pmatrix}1\\0\\0\end{pmatrix}\hat{\boldsymbol{x}}_0^{\mu T}\boldsymbol{\Phi}_{2,1\text{-}6}^T\boldsymbol{\Phi}_{2,1\text{-}5} \right) \cdot \tilde{\boldsymbol{x}}_0 =$$

$$\boldsymbol{u}_i \times \left(\mu\left(-\boldsymbol{\Phi}_{1\text{-}3,6} + \frac{1}{R}\begin{pmatrix}1\\0\\0\end{pmatrix}\hat{\boldsymbol{x}}_0^{\mu T}\boldsymbol{\Phi}_{2,1\text{-}6}^T\Phi_{2,6} \right) + \boldsymbol{q}(\hat{\boldsymbol{x}}_0^\mu) \right), i \in [1,n] \tag{26}$$

However it has to be recalled that, following this strategy, the minimum of $\sum_{i=1}^n \|\boldsymbol{r}(t_i,\boldsymbol{x}_0) \times \boldsymbol{u}_i\|^2$ would then been obtained instead of the minimum of $J = \sum_{i=1}^n \|\boldsymbol{h}(t_i,\boldsymbol{x}_0) \times \boldsymbol{u}_i\|^2$. Thus, Eq. 26 has to be divided by the norm of the relative position, which can be approximated as

$$r^\mu \approx \|\boldsymbol{I}_{\mathrm{r}}\hat{\boldsymbol{x}}_0^\mu\| = |\mu|\left\|\boldsymbol{I}_{\mathrm{r}}\boldsymbol{A}_{\mathrm{L}}^+\boldsymbol{b}_{\mathrm{L}}\right\|. \tag{27}$$

where $\boldsymbol{I}_{\mathrm{r}} = \begin{pmatrix}\boldsymbol{I}_{3\times3} & \boldsymbol{0}_{3\times3}\end{pmatrix}$ is a simple identity matrix returning only the relative position. After accumulating n measurements, another linear system is again obtained:

$$\boldsymbol{A}(\mu)\tilde{\boldsymbol{x}}_0 = \boldsymbol{b}(\mu) \tag{28}$$

28

for which the minimum can be analytically computed. Remember that $\boldsymbol{A}$ and $\boldsymbol{b}$ depend on μ because they are function of $\hat{\boldsymbol{x}}_0^\mu$. The minimum $m(\mu)$ of $\left\|\boldsymbol{A}(\mu)\tilde{\boldsymbol{x}}_0 - \boldsymbol{b}(\mu)\right\|^2$ is obtained introducing the solution $\hat{\tilde{\boldsymbol{x}}}_0^\mu$ in the loss function:

$$m(\mu) = \left\|\boldsymbol{A}(\mu)\hat{\tilde{\boldsymbol{x}}}_0^\mu - \boldsymbol{b}(\mu)\right\|^2 \tag{29}$$

$$= (\boldsymbol{A}(\mu)\hat{\tilde{\boldsymbol{x}}}_0^\mu - \boldsymbol{b}(\mu))^T(\boldsymbol{A}(\mu)\hat{\tilde{\boldsymbol{x}}}_0^\mu - \boldsymbol{b}(\mu)) \tag{30}$$

$$= \boldsymbol{b}(\mu)^T(\boldsymbol{P}(\mu) - \boldsymbol{I})^2\boldsymbol{b}(\mu) \tag{31}$$

$$= \boldsymbol{b}(\mu)^T(\boldsymbol{I} - \boldsymbol{P}(\mu))\boldsymbol{b}(\mu) \tag{32}$$

where the projection matrix $\boldsymbol{P}(\mu) = \boldsymbol{A}(\mu)(\boldsymbol{A}(\mu)^T\boldsymbol{A}(\mu))^{-1}\boldsymbol{A}(\mu)^T$ has been introduced for simplicity.

An analytical formulation of the minimum in the least-squares sense of the loss function when μ is arbitrarily fixed has now been derived. Its convexity has still to be demonstrated. Deriving the analytical formulation of $\boldsymbol{P}(\mu)$ would be extremely tedious. Fortunately, it is possible to simplify Eq. 26 in order to approximate $\boldsymbol{A}(\mu)$ by considering that :

$$\left\|\boldsymbol{\Phi}_{1,1\text{-}5}\right\| >> \frac{1}{R}\left\|\hat{\boldsymbol{x}}_0^{\mu T}\boldsymbol{\Phi}_{2,1\text{-}6}^T\boldsymbol{\Phi}_{2,1\text{-}5}\right\| \tag{33}$$

This assumption is easily justified: $\boldsymbol{\Phi}_{2,1\text{-}6}\hat{\boldsymbol{x}}_0^\mu$ is nothing else than the along-track component of the propagated linear solution using a linear relative motion model, which amounts to a few dozen kilometers in the problem under consideration, while R is the orbit radius. Consequently, the left part of the inequality is three order of magnitude larger than the right part. Recalling that Eq. 26 has been divided by r^μ, this allows us to assume that $\boldsymbol{A}(\mu)$ is inversely proportional to $|\mu|$ (that is $\boldsymbol{A}(\mu) \approx \frac{1}{|\mu|}\boldsymbol{A}$) and that $\boldsymbol{P}(\mu) \approx \boldsymbol{A}\boldsymbol{A}^+ = \boldsymbol{P}$, which does not depend on μ anymore. The expression of $\boldsymbol{b}(\mu)$ can be more easily derived. Introducing Eq. 23 in Eq. 26, the contribution $\boldsymbol{b}_i$ of a single measurement to the vector $\boldsymbol{b}$ is:

$$\boldsymbol{b}_i = \frac{1}{|\mu|\left\|\boldsymbol{I}_r\boldsymbol{A}_L^+\boldsymbol{b}_L\right\|}\boldsymbol{u}_i \times \mu\left(-\boldsymbol{\Phi}_{1\text{-}3,6} + \frac{1}{R}\begin{pmatrix}1\\0\\0\end{pmatrix}\mu\left(\boldsymbol{A}_L^+\boldsymbol{b}_L\right)^T\boldsymbol{\Phi}_{2,1\text{-}6}^T\boldsymbol{\Phi}_{2,6}\right)$$

$$- \frac{1}{|\mu|\left\|\boldsymbol{I}_r\boldsymbol{A}_L^+\boldsymbol{b}_L\right\|}\boldsymbol{u}_i \times \frac{1}{2R}\begin{pmatrix}1\\0\\0\end{pmatrix}\mu^2\left(\boldsymbol{A}_L^+\boldsymbol{b}_L\right)^T\boldsymbol{\Phi}_{2,1\text{-}6}^T\boldsymbol{\Phi}_{2,1\text{-}6}\boldsymbol{A}_L^+\boldsymbol{b}_L, i \in [1,n]$$

$$\tag{34}$$

29

Thus, the vector $\boldsymbol{b}$ can be expressed in the form:

$$\boldsymbol{b} = \operatorname{sign}(\mu)(\boldsymbol{b}_1 + \mu\boldsymbol{b}_2) \tag{35}$$

and, by introducing for simplicity $\boldsymbol{M} = (\boldsymbol{I} - \boldsymbol{P})$, the minimum becomes

$$m(\mu) = \boldsymbol{b}_1^T \boldsymbol{M} \boldsymbol{b}_1 + \mu^2 \boldsymbol{b}_2^T \boldsymbol{M} \boldsymbol{b}_2 + 2\mu \boldsymbol{b}_1^T \boldsymbol{M} \boldsymbol{b}_2 \tag{36}$$

The convexity of the function $m(\mu)$ is verified using the second order derivative, which is positive because $\boldsymbol{M}$ is semi-definite positive, yielding $\frac{d^2 m(\mu)}{d\mu^2} = \boldsymbol{b}_2^T \boldsymbol{M} \boldsymbol{b}_2 \geq 0$. Consequently, the minimum function is convex and reaches its minimum for

$$\hat{\mu} = -\frac{\boldsymbol{b}_1^T \boldsymbol{M} \boldsymbol{b}_2}{\boldsymbol{b}_2^T \boldsymbol{M} \boldsymbol{b}_2} \tag{37}$$

Interestingly, an approximate value for $\hat{\mu}$ is analytically provided as by-product. This could be extremely valuable in case there is no time to perform the series of nonlinear least-square estimations (typically for onboard implementation). In this case, it would be enough to choose an arbitrary value for μ, to linearize around the associated linear solution and to directly retrieve the approximate value of $\hat{\mu}$. The performance of this direct method will be investigated in more detail in future work.

References

Ardaens, J.S., D'Amico, S., Montenbruck, O., 2012. Final Commissioning of the PRISMA GPS Navigation System. Journal of Aerospace Engineering, Sciences and Applications 4, 104–118.

Ardaens, J.S., Gaias, G., 2018a. Angles-Only Relative Orbit Determination in Low Earth Orbit. Advances in Space Research 31, 2740–2760. 10.1016/j.asr.2018.03.016.

Ardaens, J.S., Gaias, G., 2018b. Flight Demonstration of Spaceborne Real-Time Angles-Only Navigation to a Noncooperative Target in Low-Earth Orbit. Acta Astronautica 153, 367–382. 10.1016/j.actaastro.2018.01.044.

Baumann, F., Trowitzsch, S., Brieß, K., 2012. BEESAT - A CubeSat Series Demonstrates Novel Picosatellite Technologies, 4th European CubeSat Symposium, Brussels, Belgium.

de Bruijn, F., Gill, E., How, J.H., 2011. Comparative analysis of Cartesian and curvilinear Clohessy-Wiltshire equations. Journal of Aerospace Engineering, Sciences and Applications 3.

Chari, R.J.V., 2001. Autonomous Orbital Rendezvous Using Angles-Only Navigation. Ph.D. thesis. Massachusetts Institute of Technology. Dept. of Aeronautics and Astronautics.. U.S.A.

D'Amico, S., Ardaens, J.S., Gaias, G., Benninghoff, H., Schlepp, B., Jørgensen, J.L., 2013. Noncooperative Rendezvous Using Angles-Only Optical Navigation: System Design and Flight Results. Journal of Guidance, Control, and Dynamics 36, 1576–1595. Doi: 10.2514/1.59236.

Delpech, M., Berges, J.C., Djalal, S., Christy, J., 2012. Vision Based Rendezvous Experiment performed during the PRISMA Extended Mission, in: Proceedings of the 23$^{\mathrm{rd}}$ International Symposium on Space Flight Dynamics, Jet Propulsion Laboratory, Pasadena, California, USA.

Gaias, G., Ardaens, J.S., 2018. Flight Demonstration of Autonomous Noncooperative Rendezvous in Low Earth Orbit. Journal of Guidance, Control, and Dynamics 41, 1137–1354. Https://doi.org/10.2514/1.G003239.

Gaias, G., Ardaens, J.S., Montenbruck, O., 2015. Model of J2 Perturbed Satellite Relative Motion with Time-Varying Differential Drag. Celestial Mechanics and Dynamical Astronomy 123, 411–433. Doi: 10.1007/s10569-015-9643-2.

Gaias, G., D'Amico, S., Ardaens, J.S., 2014. Angles-Only Navigation to a Noncooperative Satellite Using Relative Orbital Elements. Journal of Guidance, Control, and Dynamics 37, 439–451. Doi: 10.2514/1.61494.

Garg, S., Sinclair, A., 2015. Initial Relative-Orbit Determination Using Second-Order Dynamics and Line-of-Sight Measurements, 25$^{\mathrm{th}}$ AAS/AIAA Space Flight Mechanics Meeting, Williamsburg, Virginia.

Gauss, C.F., 1809. Theory of the Motion of the Heavenly Bodies Moving about the Sun in Conic Sections: a translation of Gauss's "Theoria motus.". (English translation, Little, Brown and company).

Geller, D.K., Klein, I., 2014. Angles-Only Navigation State Observability During Orbital Proximity Operations. Journal of Guidance, Control, and Dynamics 37, 1976–1983. Doi: 10.2514/1.G000133.

Geller, D.K., Lovell, T.A., 2017. Angles-Only Initial Relative Orbit Determination Performance Analysis using Cylindrical Coordinates. The Journal of the Astronautical Sciences 64, 72–96. doi:10.1007/s40295-016-0095-z.

Gim, D.W., Alfriend, K.T., 2003. State Transition Matrix of Relative Motion for the Perturbed Noncircular Reference Orbit. Journal of Guidance, Control and Dynamics 26, 956–971.

Grzymisch, J., Fichter, W., 2014a. Analytic Optimal Observability Maneuvers for In-Orbit Bearings-Only Rendezvous. Journal of Guidance, Control, and Dynamics 37, 1658–1664. Doi: 10.2514/1.G000612.

Grzymisch, J., Fichter, W., 2014b. Observability Criteria and Unobservable Maneuvers for In-Orbit Bearings-Only Navigation. Journal of Guidance, Control, and Dynamics 37, 1250–1259. Doi: 10.2514/1.62476.

Halle, W., Bärwald, W., Terzibaschian, T., Schlicker, M., Westerdorf, K., 2014. The DLR -Satellite BROS in the Fire-Bird Mission, in: Proceedings of the 4S Symposium: Small Satellites, Systems and Services, 26 - 30 May 2014, Majorca, Spain. European Space Agency, Noordwijk, The Netherlands.

Jørgensen, J., Denver, T., Betto, M., Jørgensen, P., Röser, H.P., Sandau, R., Valenzuela, A., 2003. The Micro ASC, a Miniature Star Tracker, Small Satellites for Earth Observation, 4th International Symposium of the International Academy of Astronautics. pp. 157–162.

Kahle, R., Weigel, M., Kirschner, M., Spiridonova, S., Kahr, E., Letsch, K., 2014. Relative Navigation to Non-cooperative Targets in LEO: Achievable Accuracy from Radar Tracking Measurements. Int. J. Space Science and Engineering 2, 81–95.

Liou, J.C., 2011. An active debris removal parametric study for LEO environment remediation. Advances in Space Research 47, 1865–1876.

Liou, J.C., Johnson, N., 2008. Instability of the present LEO satellite populations. Advances in Space Research 41, 1046 – 1053. Doi: 10.1016/j.asr.2007.04.081.

Lovell, T.A., Tragesser, S.G., 2004. Guidance for relative motion of low earth orbit spacecraft based on relative orbit elements, AIAA Guidance, Navigation and Control Conference and Exhibit, Providence, Rhode Island, USA.

Noteborn, R., Bodin, P., Larsson, R., Chasset, C., 2011. Flight Results from the PRISMA Optical Line of Sight Based Autonomous Rendezvous Experiment, in: Proceedings of the 4th International Conference on Spacecraft Formation Flying Missions & Technologies (SFFMT), Canadian Space Agency, St-Hubert, Quebec.

Perez, A.C., 2017. Applications of Relative Motion Models Using Curvilinear Coordinate Frames. Ph.D. thesis. Utah State University. U.S.A.

Persson, S., Jakobsson, B., Gill, E., 2005. PRISMA - Demonstration Mission for Advanced Rendezvous and Formation Flying Technologies and Sensors, 56th International Astronautical Congress, Fukuoka, Japan.

Sullivan, J., D'Amico, S., 2017. Nonlinear Kalman Filtering for Improved Angles-Only Navigation Using Relative Orbital Elements. Journal of Guidance, Control, and Dynamics 40, 2183–2200. Doi: 10.2514/1.G002719.

Sullivan, J., Koenig, A., D'Amico, S., 2016. Improved Maneuver-Free Approach to Angles-Only Navigation for Space Rendezvous, 26th AAS/AIAA Space Flight Mechanics Conference, Napa, California.

Woffinden, D.C., 2008. Angles-Only Navigation for Autonomous Orbital Rendezvous. Ph.D. thesis. Utah State University. U.S.A.

Woffinden, D.C., Geller, D.K., 2009a. Observability Criteria for Angles-Only Navigation. IEEE Transactions on Aerospace and Electronic Systems 45, 1194–1208.

Woffinden, D.C., Geller, D.K., 2009b. Optimal orbital rendezvous maneuvering for angles-only navigation. Journal of Guidance, Control, and Dynamics 32, 1382–1387.

33